

## Fatigue Crack Propagation in A533B Steels

A. D. WILSON

Research Engineer,  
Research Division,  
Lukens Steel Company,  
Coatesville, Pennsylvania

*The influence of steelmaking practice on the fatigue crack propagation behavior of A533B low alloy plate steels is examined. Conventional practice, calcium-treated and electroslag-remelted steels were investigated in 6 specimen orientations. A significant improvement in the isotropy of fatigue crack growth rates and a consistent overall improvement in fatigue crack growth rate were found in going from the conventional practice, to the calcium-treated, to the electroslag-remelted materials. The fatigue crack growth rate differences within a material and between materials were attributed to material differences in nonmetallic inclusion quantities and morphologies.*

### Introduction

A533B Class 1 steel plate is the basic material used in current designs of primary reactor pressure vessels, steam generators and pressurizers in nuclear power plants. This Mn-Mo-Ni low alloy steel of 50 ksi (344.5 MN/m<sup>2</sup>) minimum 0.2 percent yield strength is used in these applications up to 12 in. (304.8mm) thick. Extensive investigatory work has been done in determining the properties and behavior of this material. The Heavy Section Steel Technology (HSST) program was a major cooperative government-industry effort, in which A533B was a primary material for study. In particular, the determination of the reliability of nuclear pressure vessels of resisting catastrophic failure required extensive determinations of fracture mechanics material properties of A533B. These studies lead to the lower bound fracture toughness curve and upper bound fatigue crack growth rate curve that are given in the ASME Code [1].<sup>1</sup>

Because of the tremendous amount of testing of the specific chemistry of A533B, particularly of irradiation effects, there is a natural hesitancy for further improvement of the steel by alloying. Also the continued improvement of the properties of steels through alloying and heat treatment has recently been hampered by the escalation of costs of alloying elements, oil and natural gas. This has given additional impetus to improving steel quality through the use of advanced steelmaking techniques, which involve decreasing the amount and controlling the shape and distribution of sulphur and other nonmetallic indigenous inclusions in steel. Our production efforts with these advanced steelmaking techniques have concentrated on A533B Class 1 plate. The investigations have ranged from low sulfur furnace charges to various slagging operations, to certain ladle additions (calcium, rare earth metals and mixtures with calcium), to electroslag remelting (ESR). The ESR technique has been found to be the best for improving the quality of A533B steel [2].

The anisotropy and directionality of mechanical properties in steel has been studied and reported extensively. The major cause of anisotropy is the presence of nonmetallic inclusions, which during the solidification and hot working processes either assume specific orientations with respect to the metal matrix or are deformed under hot working. In A533B steel, manganese sulfide and alumina inclusions are the major causes of directionality [3]. The previously mentioned steelmaking practices either lower the amount of the inclusions or lead to modification of the existing inclusions, so that they are harder at hot working temperatures and resist deformation (shape control). Although some work has shown the benefits to be gained in the levels and isotropy of fracture toughness and charpy V-notch (CVN) impact properties for some of these techniques [2], no extensive fatigue crack propagation (FCP) studies have been made.

With the above introduction in mind, materials from three A533B Class 1 production plates were chosen for a fatigue crack propagation study. One material was from a conventional practice, moderate sulphur level heat, one was from a calcium treated heat and the other material was from an ESR heat. The objectives of the program in studying these materials were: to obtain FCP property data on recent A533B material using the most up-to-date testing and analytical techniques, to document differences, if any, in the FCP properties of material made by different steelmaking practices, and to establish the extent of the anisotropy of FCP in A533B and its variation in material made by different steelmaking practices.

### Experimental Procedure

**Materials.** Material from three production heats were used in this study. The chemical analyses and the thicknesses of the three plates are given in Table 1. The heat treatment each plate material received is given in Table 2.

For purposes of simplification, the materials will be referred to by the last two digits of the heat number, namely, 75, 61, and 48. The choosing of these particular heats allows the comparison of two steels of identical sulphur level, with one having calcium induced inclusion shape control. These can then be compared to the third low sulphur ESR material.

<sup>1</sup>Numbers in brackets designate References at end of paper.

Contributed by the Pressure Vessels and Piping Division and presented at the Winter Annual Meeting, New York, New York, December 5-10, 1976, of THE AMERICAN SOCIETY OF MECHANICAL ENGINEERS. Manuscript received at ASME Headquarters, July 22, 1976. Paper No.-76 WA/PVP-6.

**Table 1. Chemistry (weight percent)**

		C	Mn	P	S	Si	Cu	Ni	Cr	Mo	Al	Plate in.	thickness (mm)
B6075	Heat	0.21	1.36	0.004	0.013	0.24	0.13	0.50	0.10	0.50	0.015	6-7/16	(164)
	Product	0.18	1.41	0.008	0.009	0.23	0.13	0.48	0.11	0.48	0.045		
C3561	Heat	0.19	1.16	0.010	0.012	0.18	0.11	0.61	0.07	0.54	0.039	7-3/8	(187)
	Product	0.20	1.27	0.012	0.009	0.18	0.11	0.61	0.08	0.55	0.046		
R0048	Heat	0.25	1.47	0.013	0.005	0.14	0.10	0.51	0.11	0.59	0.011	6	(152)
	Product	0.24	1.44	0.011	0.002	0.15	0.12	0.49	0.09	0.60	0.017		

**Table 2. Heat treatment**

B6075	1650°F (899°C) - 7 - WQ + 1240°F (671°C) - 7 - AC + 1100°F (593°C) - 40 - FC
C3561	1650°F (899°C) - 7 - WQ + 1240°F (671°C) - 7 - AC + 1150°F (621°C) - 37 - FC
R0048	1650°F (899°C) - 6 - WQ + 1280°F (693°C) - 6 - AC + 1100°F (593°C) - 40 - FC

(Temperature—time in hr—cooling)

WQ—water quenching, AC—air cooling, FC—furnace cooling

**Testing Orientations and Location.** In order to extensively determine the anisotropy of properties in these plates, all possible specimen orientations were studied. For tensile testing, this meant tests in the 3 principal orientations with respect to the major rolling direction. For CVN impact and FCP tests this meant 6 separate orientations, namely each of 2 possible cracking directions in each of the 3 possible specimen orientations. Fig. 1 shows all of the specimen orientations. The identification convention used is that suggested in ASTM E399. The 3 principal directions being L, in the rolling direction, T, transverse to the rolling direction, and S, through thickness. The first letter of the specimen identification indicates the general alignment of the axis and the second letter indicates the cracking direction. Testing in the LS and TS orientations is not normally done, however, since cracks in pressure vessels propagate into the thickness of the vessel, as well as extending in length, this information would be of direct interest. The testing and metallographic specimens were centered at approximately two inches from the surface of the plate.

**Mechanical Properties.** The tensile properties were determined for the 3 materials in each of the 3 orientations on 0.252-

in-dia specimens. The results are given in Table 3. CVN impact properties were determined in each of the 6 possible orientations. Table 4 summarizes specific CVN data of interest. The isotropy of tensile ductility and impact toughness is shown to improve from heat 75 to 61 to 48. This indicates that use of inclusion shape control helps in reducing directionality, however, a low sulphur level gives the most isotropic material in ductility and in impact toughness testing. It is also interesting to note that in material 75 there was also an effect of notch direction in both the longitudinal and transverse specimens, particularly as measured in upper shelf CVN energy. This was not the case for the improved heats 61 to 48.

**Metallography.** The microstructures of all three heats were studied in each of the three possible cross sections relative to the rolling direction at about 2 in. below the plate surface. The prior austenitic grain sizes of all three materials in all 3 orientations were about ASTM 6-8. This was difficult to establish more accurately because all 3 materials displayed a tempered structure and also the presence of banding that is commonly found in this material. There were however, no consistent or significant grain size differences between or within the testing materials.

The inclusion structures in the three materials were quantified as shown in Table 5.<sup>2</sup> There is a demonstrated improvement in steel cleanliness in going from material 75 to 61 to 48. The types of inclusions present were also established. The conventional practice heat 75 had the Type II interdendritic manganese sulfide [4] and alumina inclusions typical of steel with this deoxidation practice. Figs. 2 and 3 show composite unetched micrographs of the three cross sections displaying these inclusions. In Fig. 2 the Type II MnS inclusions are shown with their strung-out nature in the directions of major rolling and crossrolling. The pancaked effect that rolling gives these inclusions is particularly indicated in the view looking from the top of the plate into the thickness of the plate. The alumina galaxies in material 75 are shown in Fig. 3. These galaxies do have small rounded MnS inclusions also associated with them. Although the individual inclusions in these galaxies are not individually deformed, the process of rolling tends to align the galaxies in a planar fashion. Both types of inclusions undoubtedly lead to the anisotropy of ductility and impact toughness mentioned previously in material 75.

<sup>2</sup>Extensive metallographic examinations, including use of quantitative image analysis, and fractographic investigations were performed in conjunction with the work presented here. It is felt that these studies are outside the intended scope of this paper and they will instead be presented in a future publication. A small portion of this work is provided here to assist in the discussions.

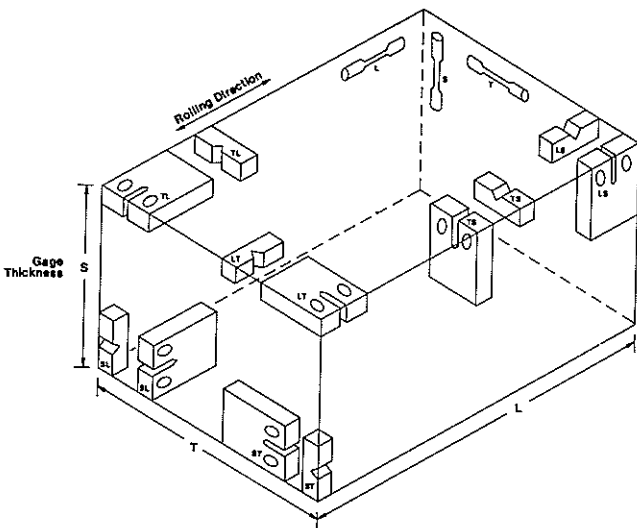


**Fig. 1 Schematic drawing showing specimen orientations for fatigue crack propagation and CVN impact testing**

**Table 3 Tensile properties (a)**

		0.2 YS (1)	UTS (2)	% El (3)	% RA (4)
B6075	L	64.4 (444)	85.4 (589)	29.0	71.4
	T	63.2 (436)	84.9 (585)	25.3	57.5
	S <sup>(b)</sup>	63.7 (439)	80.2 (553)	9.8	20.3
C3561	L	71.7 (494)	87.5 (603)	27.9	72.8
	T	71.7 (494)	87.2 (601)	27.0	70.2
	S	71.9 (496)	87.2 (601)	25.5	66.9
R0048	L	75.7 (532)	97.0 (669)	25.2	71.9
	T	74.9 (516)	96.0 (662)	26.5	72.8
	S	74.4 (513)	94.5 (652)	25.0	68.7

(a) Average of two 0.252-in- (6.4-mm-) dia tests

(b) Only one specimen

(1) 0.2YS 0.2 percent offset yield strength, ksi (MN/m<sup>2</sup>)

(2) UTS Ultimate tensile strength, ksi (MN/m<sup>2</sup>)

(3) % El Percent elongation in 1 in.

(4) % RA Percent reduction of area

L Longitudinal

T Transverse

S Through thickness

**Table 4 Summary of CVN Impact properties (4)**

	Orient.	Upper shelf (1)		Room temperature (2)		FATT (3)	
		Energy	Lateral ex.	Energy	Lateral ex.		
B6075	LS	150 (203)	87 (2.2)	139 (188)	88 (2.2)	-15	(-25)
	LT	127 (172)	89 (2.3)	119 (161)	85 (2.2)	+15	(-9.4)
	TS	85 (115)	75 (1.9)	74 (100)	68 (1.7)	+15	(-9.4)
	TL	85 (115)	66 (1.7)	67 (91)	60 (1.5)	+25	(-3.9)
	ST	43 (58)	46 (1.2)	31 (42)	34 (0.86)	+35	(+1.7)
	SL	40 (54)	48 (1.2)	36 (49)	40 (1.0)	+40	(+4.4)
C3561	LS	137 (186)	94 (2.4)	119 (161)	81 (2.1)	+15	(-9.4)
	LT	141 (191)	95 (2.4)	144 (195)	94 (2.4)	+10	(-12)
	TS	127 (172)	95 (2.4)	108 (146)	82 (2.1)	+25	(-3.9)
	TL	128 (174)	94 (2.4)	102 (138)	82 (2.1)	+20	(-6.7)
	ST	96 (130)	82 (2.1)	72 (98)	63 (1.6)	+45	(+7.2)
	SL	94 (127)	80 (2.0)	73 (99)	63 (1.6)	+40	(+4.4)
R0048	LS	129 (175)	89 (2.3)	120 (163)	81 (2.1)	+30	(-1.1)
	LT	137 (186)	93 (2.4)	118 (160)	82 (2.1)	+25	(-3.9)
	TS	127 (172)	88 (2.2)	94 (127)	70 (1.8)	+45	(+7.2)
	TL	127 (172)	88 (2.2)	98 (133)	71 (1.8)	+20	(-6.7)
	ST	125 (169)	88 (2.2)	96 (130)	73 (1.9)	+35	(+1.7)
	SL	143 (194)	94 (2.4)	87 (118)	68 (1.7)	+60	(+16)

(1) Upper shelf properties—average values at 100 percent ductile of absorbed energy, ft-lb (J) and lateral expansion, mils(mm)

(2) Room Temperature properties—average of 2 tests of absorbed energy, ft-lb (J) and lateral expansion, mils(mm)

(3) Fracture appearance transition temperature at 50 percent ductile, °F(°C)

(4) Standard 10mm square cross-section specimens

**Table 5 Inclusion rating (a)**

	Orient.	Sulfide		Alumina		Silicate		Globular		Nitride	
		A		B		C		D		E	
		T	H	T	H	T	H	T	H	T	H
B6075	Top	3	2.5	2	5	0	0	1	1	0	0
	End	1.5	0	2.5	2.5	0	0	1.5	1.5	0	0
	Side	3	2	2	2	0	0	1	1	0	0
C3561	Top	1.5	2	0	0	0	0	1.5	1.5	0	0
	End	2	1.5	0	0	0	0	1.5	1.5	Trace	0
	Side	2	1.5	0	0	0	0	1.5	1.5	0	0
R0048	Top	0.5	0.3	0	0	0	0	1	0.5	0	0
	End	1	0.3	0.5	0.5	0	0	1.5	1	0	0
	Side	1	0.3	0.3	1	0	0	1.5	1	0	0

(a) Using ASTM E-45 Microscope Method A

T = Thin

H = Heavy

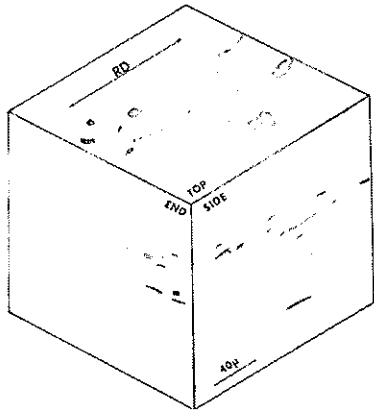


Fig. 2 Composite of light photomicrographs from conventional practice material B6075 indicating morphology of largest Type II manganese sulfide inclusions

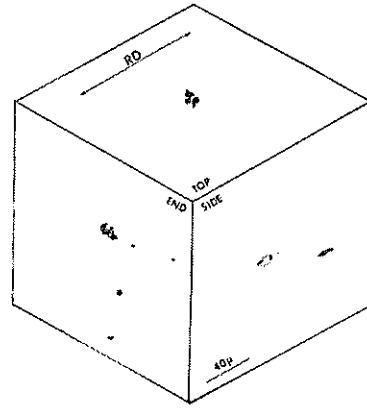


Fig. 5 Composite of light photomicrographs from ESR material R0048 indicating morphology of largest modified and unmodified inclusions

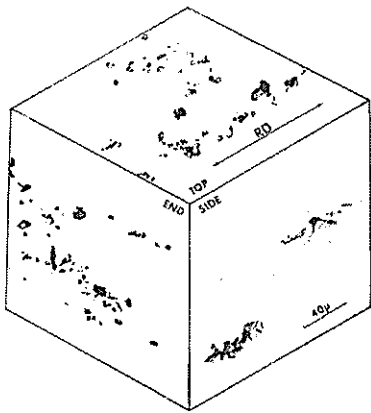


Fig. 3 Composite of light photomicrographs from conventional practice material B6075 indicating morphology of largest galaxies of alumina inclusions

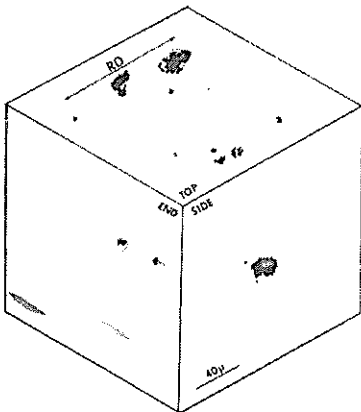


Fig. 4 Composite of light photomicrographs from calcium treated material C3561 indicating morphology of largest modified and unmodified inclusions

The calcium modified material 61 had basically 2 kinds of inclusions. The modified sulfide inclusions of a "bull's-eye" appearance are shown in Fig. 4. Unmodified MnS inclusions were also found in this steel. No alumina galaxies were found in this steel.

The ESR material 48 showed very few inclusions at all. Some calcium modified inclusions were found as shown in Fig. 5. Also some individual MnS inclusions were found.

**Fatigue Testing Procedure.** The fatigue crack propagation tests were performed on 1-in. (25.4mm) thick (1T) compact specimens of the wedge-opening-loading (WOL) design, abbreviated, 1T-WOL. In this material no consistent effect of specimen thickness has been found on FCP data [5]. The specimen dimensions are shown in Fig. 6. Because of material limitations, tests TL and SL orientations for material 61 were performed on subsized specimens with a 1-in. thickness and a specimen height to width ratio identical to that in Fig. 6. The stress intensity factor,  $K$ , calibration that was used for all specimens was that reported by Wessel [6].

The testing was performed on an electro-hydraulic, servo controlled, closed-loop testing machine at room temperature in laboratory air using a sinusoidal waveform. Pre-cracking of the notched specimens was done at room temperature in air using a sinusoidal wave form. The final pre-cracking load was between 3000 lb (13,350N) and 300 lb (1335N) at a frequency of 50 Hz. The pre-crack extended 0.10–0.15 in. (2.54–3.81mm) beyond the machined notch and was checked for straightness from both sides of the specimen prior to final testing. Maximum testing loads of both 4400 and 6000 lb (19,580 and 26,700N) were used at a loading ratio of minimum load to maximum load, of 0.1. Since this material has been found insensitive to frequency effects at room temperature in air [5], two different testing frequencies were used, 5 and 10 Hz. In order to provide as reliable data as possible, two tests were run per orientation and material. One test at 4400 lb (19,580N) maximum load and a testing frequency of 10 Hz allowed for obtaining data at low  $\Delta K$ 's, while the other test at 6000 lb (26,700N) and 5 Hz allowed for determining a higher percentage of middle to higher  $\Delta K$  data, where  $\Delta K = (K_{max} - K_{min}) =$  stress intensity factor range.

Crack length measurements were taken every 0.01 in. (0.254-mm) using an ultrasonic crack monitor of the type originated by Clark and Ceschini [7]. The ultrasonic method is particularly attractive for this study because it takes measurements at the center of the specimen where plane strain conditions exist, tends not to be as influenced by crack front curvature effects, and acts as an averaging system that will take into account a length of crack front as opposed to just surface measurements.

**Analytical Procedures.** The recommendations in the ASTM report of Clark and Hudak [8] were used extensively in planning the testing procedures and in planning and executing the data analysis. Fatigue crack growth rates ( $da/dN$ , growth in inches per cycle) were determined at each data point using the incremental polynomial technique (IPT) [8]. IPT was found to be

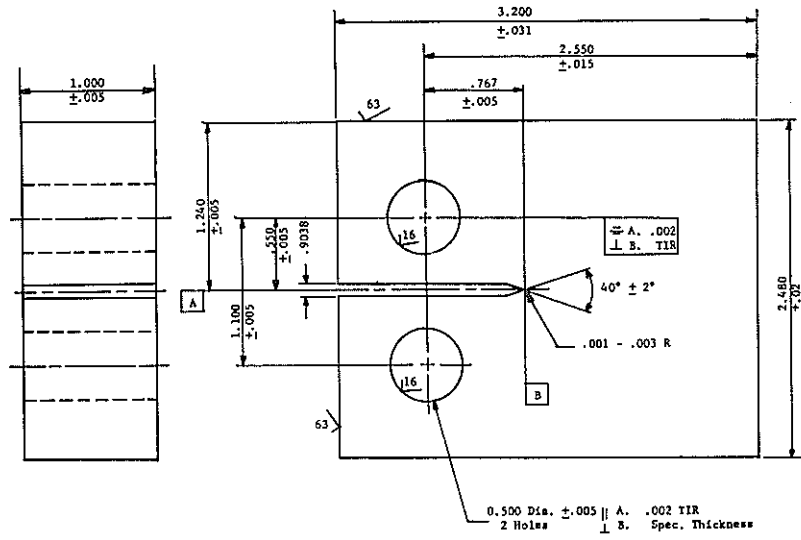


Fig. 6 IT - WOL fatigue crack propagation test specimen from reference [8]. Dimensions in in. (25.4 mm = 1 in.).

Table 6 Fatigue crack propagation data

		$n^{(a)}$	$C_0^{(b)}$	$R^2^{(c)}$	$K_{Ic}^{(d)}$	$a_{cr}^{(e)}$	$a_i^{(f)}$	$N_f^{(g)}$
B6075	LS	2.94	$2.40 \times 10^{-10}$ ( $4.62 \times 10^{-6}$ )	0.917	217(238)	18.4(467)	8.38(213)	65,500
	LT	2.84	$4.03 \times 10^{-10}$ ( $7.83 \times 10^{-6}$ )	0.972	199(219)	15.5(394)	7.34(186)	58,600
	TS	3.11	$1.23 \times 10^{-10}$ ( $2.32 \times 10^{-6}$ )	0.899	162(178)	10.2(259)	4.96(126)	53,300
	TL	3.00	$2.27 \times 10^{-10}$ ( $4.34 \times 10^{-6}$ )	0.971	162(178)	10.2(259)	4.68(119)	46,000
	ST	3.73	$2.34 \times 10^{-11}$ ( $4.19 \times 10^{-7}$ )	0.786	113(124)	4.98(126)	1.48(37.6)	16,300
	SL	3.74	$3.01 \times 10^{-11}$ ( $5.36 \times 10^{-7}$ )	0.780	109(120)	4.61(117)	1.16(29.5)	11,900
	Overall av	3.10	$1.69 \times 10^{-10}$ ( $3.22 \times 10^{-6}$ )	0.801	....	....	....	....
C3561	LS	2.88	$2.98 \times 10^{-10}$ ( $5.77 \times 10^{-6}$ )	0.952	219(241)	19.0(483)	9.13(232)	69,900
	LT	2.92	$2.56 \times 10^{-10}$ ( $4.93 \times 10^{-6}$ )	0.951	222(244)	19.5(495)	8.85(225)	66,700
	TS	3.16	$1.17 \times 10^{-10}$ ( $2.21 \times 10^{-6}$ )	0.928	211(232)	17.5(445)	6.09(155)	50,300
	TL	2.68	$7.33 \times 10^{-10}$ ( $1.45 \times 10^{-5}$ )	0.952	212(233)	17.7(450)	9.49(241)	70,100
	ST	2.79	$4.76 \times 10^{-10}$ ( $9.46 \times 10^{-6}$ )	0.969	182(200)	13.1(333)	6.88(175)	60,600
	SL	2.50	$1.49 \times 10^{-9}$ ( $3.00 \times 10^{-5}$ )	0.723	180(198)	12.8(325)	7.98(203)	70,600
	Overall av	2.91	$2.88 \times 10^{-10}$ ( $5.57 \times 10^{-6}$ )	0.938	....	....	....	....
R0048	LS	2.39	$1.96 \times 10^{-9}$ ( $3.97 \times 10^{-5}$ )	0.981	217(238)	18.5(470)	12.6(320)	97,700
	LT	2.49	$1.39 \times 10^{-9}$ ( $2.80 \times 10^{-5}$ )	0.983	224(246)	19.7(500)	12.4(315)	89,100
	TS	2.71	$6.28 \times 10^{-10}$ ( $1.24 \times 10^{-5}$ )	0.975	211(232)	17.5(445)	9.32(237)	70,300
	TL	2.61	$7.96 \times 10^{-10}$ ( $1.58 \times 10^{-5}$ )	0.976	215(236)	18.2(462)	11.2(284)	89,100
	ST	2.69	$6.05 \times 10^{-10}$ ( $1.19 \times 10^{-5}$ )	0.982	213(234)	18.0(457)	10.2(259)	79,200
	SL	2.74	$5.75 \times 10^{-10}$ ( $1.13 \times 10^{-5}$ )	0.952	229(252)	20.6(523)	10.0(254)	67,500
	Overall av	2.60	$9.08 \times 10^{-10}$ ( $1.80 \times 10^{-5}$ )	0.967	....	....	....	....

- (a) Exponent in FCP equation (1)
- (b) Coefficient in FCP equation, where units of  $\Delta K$  and  $da/dN$  are, respectively, ksi (in.)<sup>1/2</sup> and in./cycle (MN/m<sup>3/2</sup> and microns/cycle)
- (c) Statistical parameter describing effectiveness of equation (1) in fitting the actual data
- (d) Upper shelf plain strain fracture toughness calculated using Rolfe-Novak correlation [19], ksi (in.)<sup>1/2</sup> (MN/m<sup>3/2</sup>)
- (e) Critical surface flaw size for a stress of 26.7 ksi (184 MN/m<sup>2</sup>), in. (mm)
- (f) Critical initial surface flaw size that will grow to  $a_{cr}$  in 10,000 cycles of stress, in. (mm)
- (g) Number of cycles of stress required to reach  $a_{cr}$  assuming an initial surface flaw 1 in. (75.4mm) deep by 10 in. (254mm) long

the most accurate automated technique in reproducing what would be determined manually by drawing tangent lines to a hand drawn crack length-cycles curve.

Best fit straight line curves using linear regression analysis were established of the final plots of  $\log da/dN$  versus  $\log \Delta K$ . This allowed equations of the form:

$$\frac{da}{dN} = C_0(\Delta K)^n \quad (1)$$

$$C_0, n = \text{const}$$

to be established for each test. Values of  $C_0$  and  $n$  will be given in this paper. An equation of this form was found by Paris to represent FCP data [9]. Many steel, aluminum and titanium alloys have been found to generally follow this relation at inter-

mediate  $\Delta K$  and  $da/dN$  levels [10].

## Results

The results of the FCP testing are given in Figs. 7-9 for materials 75, 61 and 48, respectively. Separate graphs of the test results from each orientation are presented and the best fit straight lines of these log-log graphs in the form of equation (1) are noted in Table 6. As was expected, the data generally does appear to follow this straight line relationship on the graphs, except in some tests at very high and low stress intensity ranges. Also the  $R^2$  statistical parameters indicating the accuracy of the correlation are presented. The closer the  $R^2$  is to one, implies the better the data fits a straight line. The three materials are compared for each specific orientation in Fig. 10. Fig. 11 shows the

effect of orientation in each individual material.

These graphs indicate that the fatigue crack growth rates for the three materials compare differently depending on the orientation of the test. In the LS orientation at low  $\Delta K$ 's, material 48 has a faster growth rate than 61 or 75 and at higher  $\Delta K$ 's there is a shift to 48 having the slower growth rate. In the TS orientation at low  $\Delta K$ 's, there is a decreasing growth rate from material 48 to 61 to 75, while at higher  $\Delta K$ 's material 48 tends to have the slowest growth rate. Generally in the remaining orientations LT, TL, ST and SL there is a significant difference in growth rate only at higher  $\Delta K$ 's where there is a decreasing growth rate from material 75 to 61 to 48. There also is a significant effect of

orientation in material 75 and no consistent effect in materials 61 and 48. In material 75 the fatigue crack growth rate decreases in order by orientation as: SL, ST, LT and TL, LS and TS, with the largest differences at the higher stress intensity factor ranges.

The foregoing data are summarized in Fig. 12 for comparison of the materials using two different presentations. Fig. 12(a) compares the scatterbands of all data points for the three materials, that is, a summary of the data points given in Figs. 7-9. This graph shows a decrease in the scatter of results and a shift to slower growth rates in going from material 75 to 61 to 48, respectively. Fig. 12(b) compares the bands formed by the best fit lines for

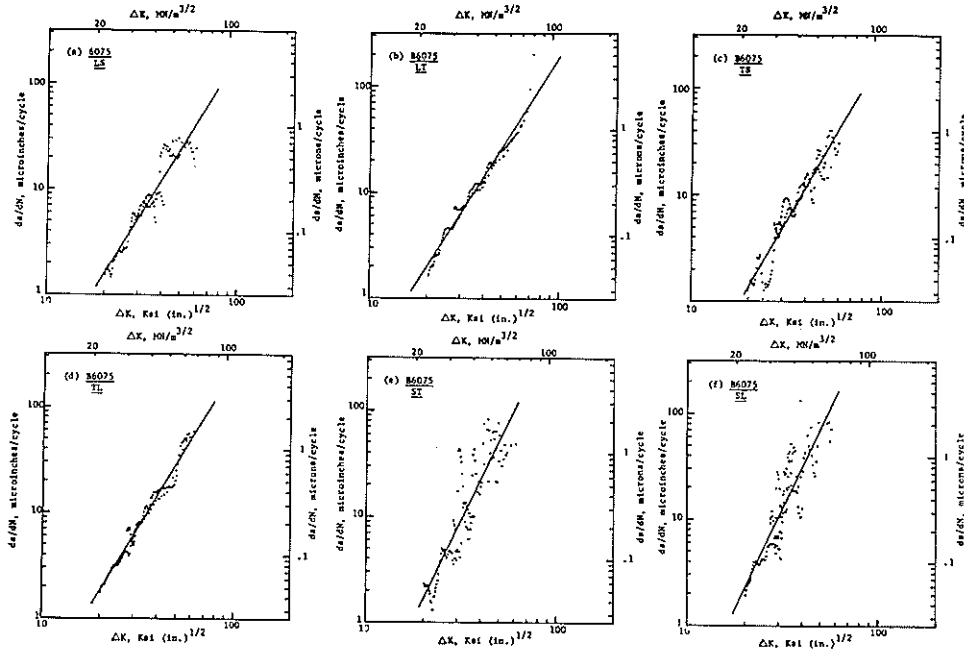


Fig. 7 Data plots of fatigue crack growth rate versus range of stress intensity factor for tests performed in each orientation for conventional practice material B6075

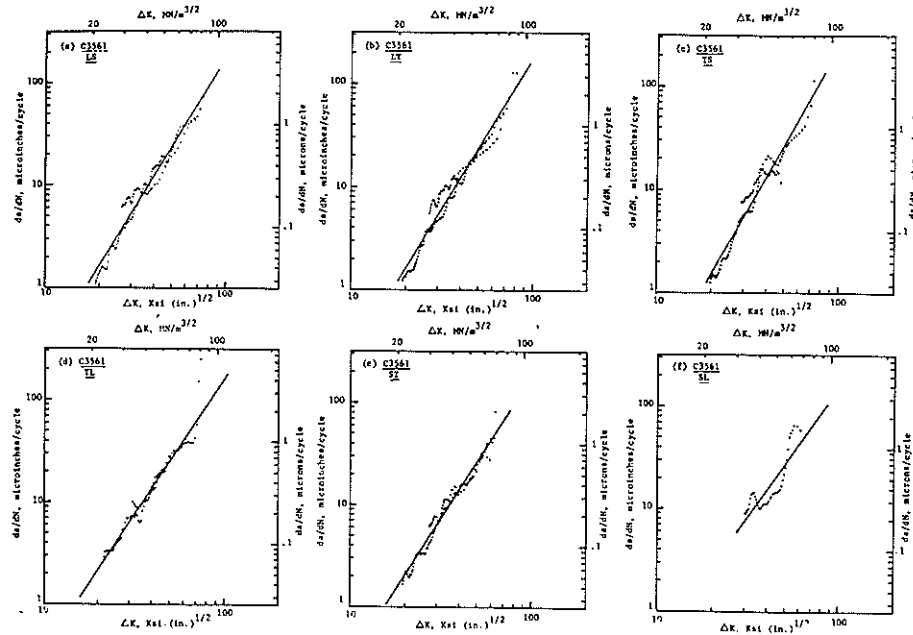


Fig. 8 Data plots of fatigue crack growth rate versus range of stress intensity factor for tests performed in each orientation for calcium-treated material C3561

each orientation of each material, i.e., a summary of Fig. 11. The spread in difference between the average growth rates of each orientation for a material decreases and the growth rates are generally slower in order from material 75 to 61 to 48, respectively, particularly at the higher stress intensity ranges.

The macroscopic appearances of the fracture surfaces of material 75 were found to be much rougher than the other materials, apparently correlating with the faster growth rate in this material. In fact, the fractures for materials 61 and 48 in the LS, LT, TS and TL orientation are almost featureless. An increasing roughness for the through-thickness orientations, ST and SL, for material 75 also appeared to correlate with the faster growth rates found for these orientations in this material.

## Discussion

**Fractography.** To understand why there are significant differences in the FCP behavior and in the macrofeatures of the fractures of the 3 materials, a fractographic study was undertaken using primarily the scanning electron microscope (SEM).<sup>3</sup> The standard practice heat 75 showed both high growth rates and rougher FCP fractures for the through-thickness specimens. There were numerous patches of the Type II manganese sulfides found as shown in Fig. 13 for an SL oriented specimen. Similarly

<sup>3</sup>See footnote 2.

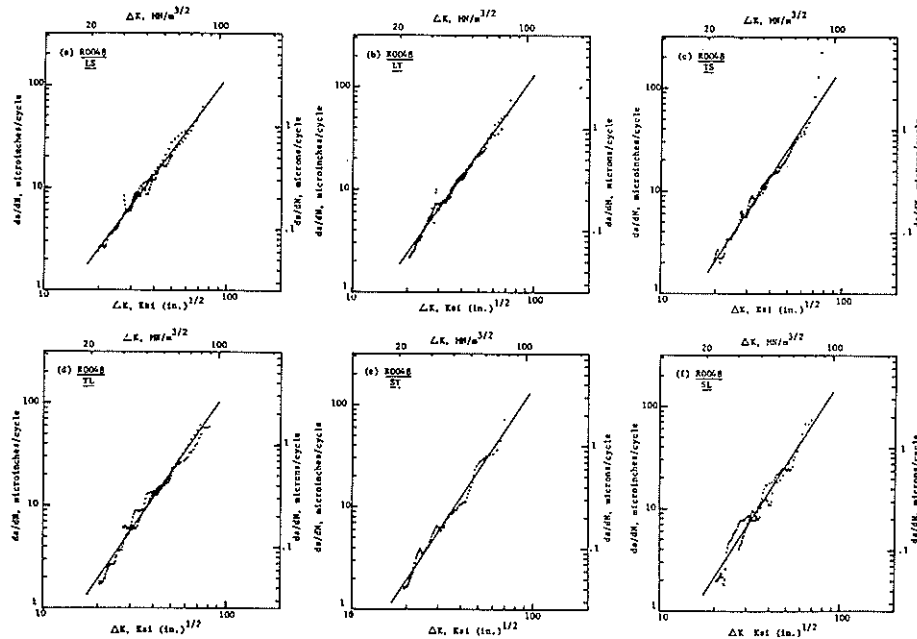


Fig. 9 Data plots of fatigue crack growth rate versus range of stress intensity factor for tests performed in each orientation for ESR material R0048

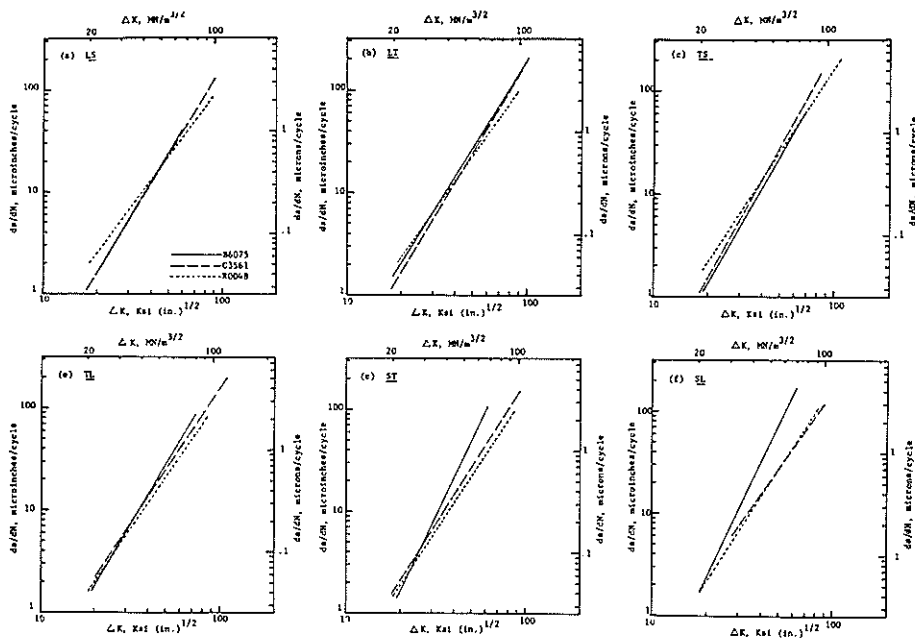


Fig. 10 Plots of fatigue crack growth rate versus range of stress intensity factor comparing the three materials in each orientation

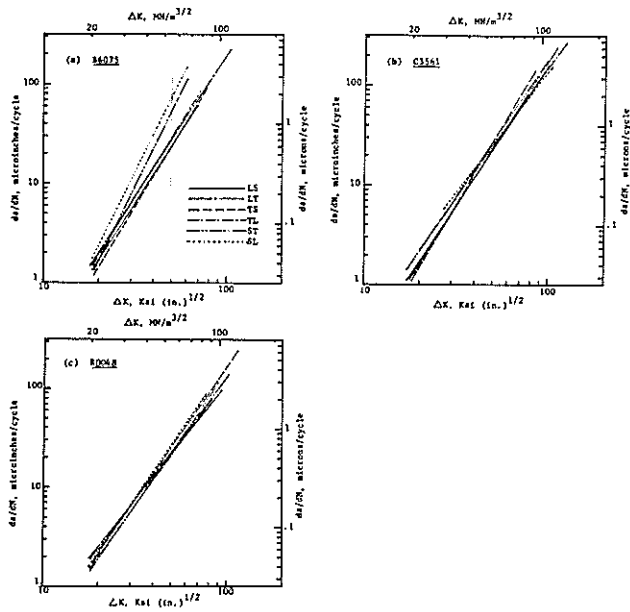


Fig. 11 Plots of fatigue crack growth rate versus range of stress intensity factor displaying the orientation differences in each of the three materials

the presence of alumina galaxies is demonstrated by Fig. 14. In both cases the patches and galaxies are appearing on several different levels. Examination of an ST oriented fracture showed similar behavior. It appears from these pictures that the inclusions in this material are the primary causes of the increased fatigue crack growth rate in through-thickness (SL or ST) testing. This would be manifested by preferential decohesion at the inclusion-matrix interface as the fatigue crack approaches an inclusion. The SL orientation showed a faster growth rate than the ST orientation because of the orientation of the MnS patches and the elongation of the MnS inclusions and alumina galaxies in the direction of rolling. This presented longer, uninterrupted crack front searched for the easiest route within its volume of influence, as determined by the plastic zone at the crack tip.

The LS and TS orientations in material 75 showed protrusions on the FCP fracture surfaces. An examination of these fractures indicated that MnS and/or alumina inclusions were present on the vertical face of these protrusions. The increased scatter and relatively slower growth rates in these orientations can be correlated with the MnS patches and alumina galaxies acting as barriers to the fatigue crack.

The LS, TS, ST and SL orientations in material 75 mentioned above, showed significant amounts of data scatter as shown in Fig. 7(a, c, e and f) and indicated by a low  $R^2$  factor for these tests. This scatter appears to take on a wavelike nature, if in-

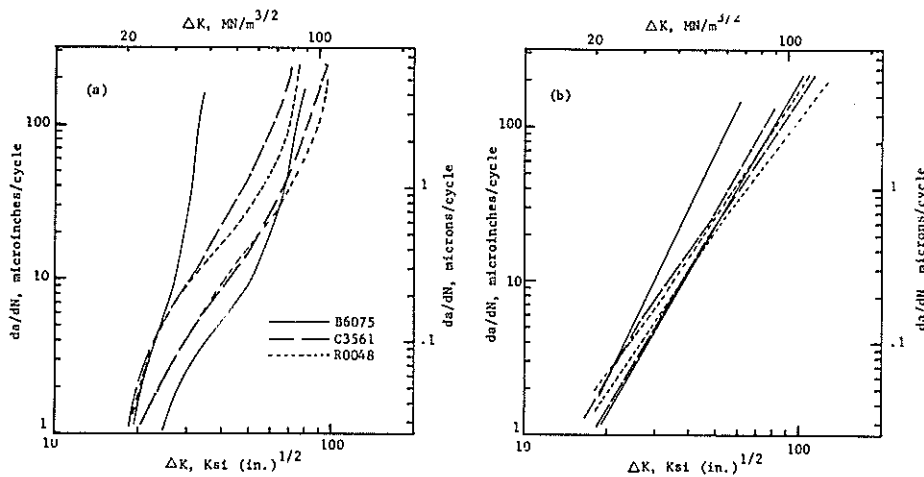


Fig. 12 Summary plots of fatigue crack growth rate versus range of stress intensity factor comparing in (a) the scatterbands encompassing all of the data points for a material, and in (b) the scatterbands encompassing all of the best fit orientation lines for a material



Fig. 13 Scanning electron micrograph of fracture surface of FCP specimen in SL orientation from conventional practice material B6075, revealing Type II manganese sulfide inclusions. The direction of crack growth is from the bottom to the top of the micrograph. This area is at the center of the specimen at a  $\Delta K$  of 27 ksi (in.)<sup>1/2</sup>.

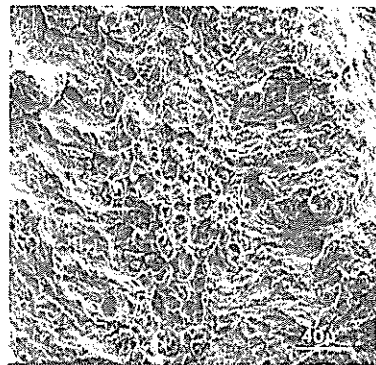


Fig. 14 Scanning electron micrograph of fracture surface of FCP specimen in SL orientation from conventional practice material B6075, revealing an alumina galaxy. The direction of crack growth is from the bottom to the top of the micrograph. This area is at the center of the specimen at a  $\Delta K$  of 27 ksi (in.)<sup>1/2</sup>.

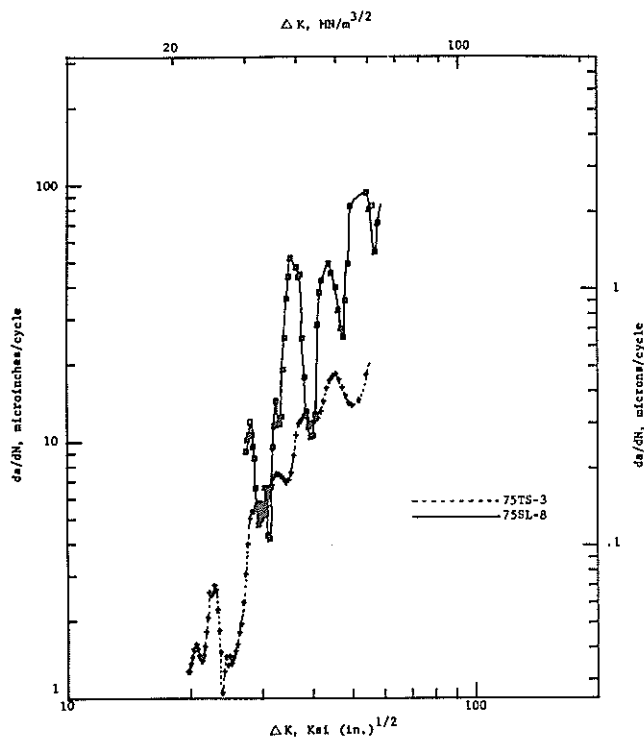


Fig. 15 Data plots of fatigue crack growth rate versus range of stress intensity factor for tests in TS and SL orientations for conventional practice material B6075

dividual tests are examined. For example, Fig. 15 shows plots of a TS and a SL orientation test. Instead of fitting a straight line to the data, a hand drawn curve joins the data points. This indicates that the fatigue crack front is alternately speeding up and slowing down during the test. It is hypothesized that this behavior in the ST and SL orientations is due to the crack front propagating faster when MnS patches or alumina galaxies are encountered and slower when propagating through the steel matrix. In the LS and TS orientations, as was mentioned previously, it appears that the crack front is slowed down when it encounters an inclusion cluster and then speeds up after by-passing the barrier. The remaining orientations for material 75, TL and LT, showed relatively less data scatter.

The calcium treated material 61 showed much less scatter than material 75 and generally slower fatigue crack growth rates. Although there was a presence of a wavelike nature to some of the data from material 61, the changes were more gradual and smoother than the erratic behavior noted in material 75. Typical MnS inclusions found on an SL oriented fracture have a polygonal shape suggesting a Type III MnS [4], as shown in Fig. 16. Qualitatively speaking, very few calcium modified inclusions were found on the fracture surfaces compared to the ease with which they were found in a metallographic cross section. The absence of the Type II MnS patches and alumina galaxies as compared to material 75, the fewer number of inclusions involved in the fatigue cracking process and the shape control of at least a portion of the inclusions present, results in the general overall lower data scatter and on the average a lower fatigue crack growth rate for the calcium treated material 61, when compared to the standard practice material 75.

The slight wavelike nature of some of the data for the ESR material 48 was less extensive and smoother than the erratic behavior noted in material 75. The through thickness fractures of this material exhibited no significant amount of inclusions. An SL oriented specimen fracture given in Fig. 17 indicates that secondary cracking and striation formation are the primary fea-

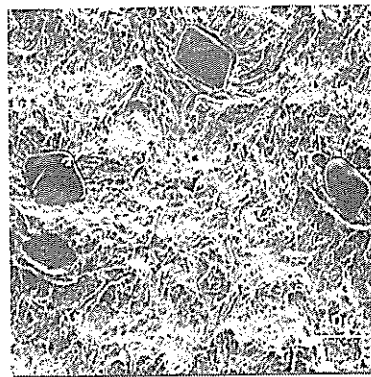


Fig. 16 Scanning electron micrograph of fracture surface of FCP specimen in ST orientation from calcium-treated material C3561 revealing polygonal shaped Type III manganese sulfide inclusions. The direction of crack growth is from the bottom to the top of the micrograph. This is at the center of the specimen at a  $\Delta K$  of 24 ksi (in.)<sup>1/2</sup>.



Fig. 17 Scanning electron micrograph of fracture surface of FCP specimen in SL orientation from ESR material R0048 revealing secondary cracking. The direction of crack growth is from the bottom to the top of the micrograph. This area is at the center of the specimen at a  $\Delta K$  of 32 ksi (in.)<sup>1/2</sup>.

tures present. The relatively little scatter in data associated with this material and the relatively low growth rate may be correlated with the very low inclusion content of this steel, when compared to materials 75 and 61.

The scatter present in testing the 3 materials, as summarized in Fig. 12, merely is a result of the orientation differences as discussed in the foregoing. Also this scatter is evident when comparing the three materials in a specific orientation by looking at the  $R^2$  parameter. For example in the LS orientation the  $R^2$  goes from 0.917 to 0.952 to 0.981 for materials 75 to 61 to 48, indicating less scatter with improved steel quality.

**Effect of Inclusions.** The work presented by this report finds areas of agreement and difference with these efforts reported in the literature [11-16]. Our work has found that there is a significant effect of inclusions, which in this particular steel was also dependent on the orientation of the test. Looking at the standard practice material, 75, alone, the significant effect of orientation on the growth rate is attributed not only to the number and size of inclusions encountered by the fatigue crack, but also to the shape and orientation of the inclusions relative to the crack front. Elongated patches and clusters of inclusions present easy paths of crack propagation in the SL and ST orientations and barriers in the TS and LS orientations. These inclusions are particularly effective in the SL and ST orientations at high stress intensity ranges, where the large plastic zone at this point in the test allows the main crack a larger volume from which to

find the easiest route, through cracking ahead of the main crack or through propagation at the inclusion-matrix interface. In the ESR material, 48, of very low inclusion content, there was no significant effect of orientation. Also in material 61 where most of the inclusions were spherical or of a more compact nature than material 75, there was no significant effect of orientation.

In comparing the 3 materials head to head, various differences were found. Looking at this comparison in certain orientations provides additional insight into the situation as shown in Fig. 10. In the LS orientation at low  $\Delta K$ 's, the ESR material, 48, has a faster growth rate than materials 75 and 61. While at higher  $\Delta K$ 's the reverse is true. This has been noted by other workers (12, 15). When inclusions are present, particularly at low growth rates and  $\Delta K$ 's, they can act as crack arrestors. This is even more so the case when the inclusions themselves can act as barriers as described previously. At higher growth rates inclusions cause an acceleration of the crack front. In the TL orientation, there were no significant material differences at low  $\Delta K$ 's, but at higher  $\Delta K$ 's the growth rate follows the trend of increasing growth rate with increasing inclusion content. In the ST and SL orientations there are no differences at low  $\Delta K$ 's, but at higher  $\Delta K$ 's the 75 material has a significantly higher growth rate, due to the patches and clusters of inclusions being preferentially oriented to accelerate fatigue crack growth in these orientations.

**Critical Crack Sizes.** In order to give an appreciation of what effect different fatigue crack growth rates can have in the design of a pressure vessel, a number of specific calculations can be made. The design practice has been generally established using fracture mechanics by various workers [17, 18].

The critical elliptical flaw size that will lead to fracture of a specific pressure vessel,  $a_{cr}$ , and the specific size of elliptical-shaped flaw that will grow to this critical size under a specific number of fatigue cycles of stress,  $a_i$ , were calculated using the formulas from the references. Also calculations were made of the number of cycles of stress required to failure,  $N_f$ , assuming a pre-existing elliptical-shaped surface flaw of 1 in. (25.4mm) deep by 10 in. (254mm) long.

For a nuclear pressure vessel, 26.7 ksi (184 MN/m<sup>2</sup>) has been established for A533B as the maximum allowable hoop stress [1]. Although this stress would not apply for all orientations of flaws in a pressure vessel it is used in our calculations for comparison purposes. The number of cycles that a vessel will see in its life depends on its specific application and the design practices of the vessel designer. However, 10,000 cycles is a conservative number that can be used for comparison purposes. A surface flaw with a depth to length ratio of 0.1 is assumed in all cases. Calculations using these formulas for the materials studied are given in Table 6. The  $K_{Ic}$  was determined from the Rolfe-Novak [19] correlation of CVN upper shelf with fracture toughness,  $K_{Ic}$ .

$$\left[ \frac{K_{Ic}}{0.2YS} \right]^2 = 5 \left[ \frac{CVN}{0.2YS} - 0.05 \right] \quad (2)$$

Where 0.2YS is the 0.2-percent yield strength in ksi and CVN is the upper shelf energy in ft-lb. All calculations were made for a case at approximately room temperature where upper shelf conditions are assumed.

The various materials and orientations can be compared in Table 6 by examining the critical flaw sizes based on one cycle of stress,  $a_{cr}$ , and 10,000 cycles of stress,  $a_i$  and by comparing  $N_f$ . In material 75 the ratio of the extreme cases, LS to SL, based only on fracture toughness conditions,  $a_{cr}$ , is 3.99. When fatigue cycling is considered, the ratio for  $a_i$  is 7.22 and by looking at the differences in  $N_f$ , it is noted that the LS orientation would withstand 53,540 more fatigue cycles. In other words, there is considerably more anisotropy in material 75 when both toughness and fatigue crack growth are considered than when just toughness is used. In going to the other materials, both larger critical initial sizes and less anisotropy is obtained. In all but one

case the ESR material gives the largest  $a_i$  and  $N_f$  values in all orientations and thus the greatest safety. When materials 48 and 61 are compared to material 75 in the SL orientation, the ratios of  $a_{cr}$  are 4.47 and 2.78, respectively. When the comparison ratios are made using  $a_i$ , one obtains 8.62 and 6.88, respectively. The differences in  $N_f$  are 55,580 and 58,670 cycles, respectively. This would indicate a much larger benefit to be obtained by going to the materials 61 and 48 than would have been obtained by just considering fracture toughness.

## Conclusions

This study of the fatigue crack propagation properties of three A533B steels, one made by conventional melting practices, another by calcium treatment and the other by electroslag remelting has concluded the following.

- 1 There is considerable anisotropy of fatigue crack growth rates in the conventional practice material.
- 2 The anisotropy in the conventional practice material was due to the presence of elongated Type II manganese sulfide inclusions and galaxies of alumina inclusions.
- 3 There is a significant improvement in the isotropy of fatigue crack growth rates in the calcium treated and electroslag remelted materials.
- 4 There is also a consistent overall improvement in fatigue crack growth rate in going from the conventional practice, to the calcium treated, to the electroslag remelted heat. There also is a decrease in testing scatter in the same order.
- 5 The fatigue crack growth rate difference within a material and between materials were attributed to the material differences in inclusion morphology and distribution.

## Acknowledgments

The author wishes to thank Mr. J. A. Gulya for his advice and guidance during the planning and writing of this paper. The efforts of Mr. T. R. Stetler in maintaining the necessary orientations during machining of the specimens are gratefully acknowledged. The fatigue crack propagation testing was done by the Westinghouse Electric Corporation, Lester, Pa. The work of Mr. J. S. Olzweski of Westinghouse in performing the fatigue crack propagation testing is particularly appreciated.

## References

- 1 ASME Boiler and Pressure Vessel Code, Sections III and XI, 1974.
- 2 Swift, R. A., and Gulya, J. A., "Property Evaluation of Electroslag Remelted A533B Plate," *Welding Research Supplement*, Dec. 1973.
- 3 Wilson, A. D., unpublished work.
- 4 Sims, C. E., and Dahle, F. B., "Effect of Aluminum on the Properties of Medium-Carbon Cast Steel," *Transactions of American Foundry Society*, Vol. 46, 1936, p. 65.
- 5 Clark, W. G., Jr., "Effect of Temperature and Section Size on Fatigue Crack Growth in A533B, Class 1 Pressure Vessel Steel," *Journal of Materials*, 6 Mar. 1971, p. 134.
- 6 Wessel, E. T., "State of the Art of the WOL Specimen for  $K_{Ic}$  Fracture Toughness Testing," *Engineering Fracture Mechanics*, Vol. I, No. 1, June 1968, p. 77.
- 7 Clark, W. G., Jr., and Ceschini, L. J., "Ultrasonic Crack Growth Monitor," *Materials Evaluation*, Aug. 1969.
- 8 Clark, W. G., Jr., and Hudak, S. J., Jr., "Variability in Fatigue Crack Growth Rate Testing," *Journal of Testing and Evaluation*, Vol. 3, No. 6, Nov. 1975, p. 454.
- 9 Paris, P. C., *Fatigue, and Interdisciplinary Approach*, Sagamore, New York, 1964, p. 107.
- 10 Clark, W. G., Jr., "How Fatigue Crack Initiation and Growth Properties Affect Material Selection and Design Criteria," *Metals Engineering Quarterly*, Aug. 1974, p. 16.
- 11 Forsyth, P. J. E., *The Physical Basis of Metal Fatigue*, American Elsevier Publishing Company, New York, 1969, p. 143.
- 12 McEvily, A. J., "Effect of Constituent Particles on the Notch-Sensitivity and Fatigue Crack Propagation Characteristics of Al-Zn-Ng Alloys," NASA TD D328, Apr. 1962.
- 13 Pelloux, R. M. N., "Fractographic Analysis of the In-

fluence of Constituent Particles on Fatigue Crack Propagation in Aluminum Alloys," *Transactions of the ASM*, Vol. 57, 1964, p. 511.

14 Brcek, D., "The Effect of Intermetallic Particles on Fatigue Crack Propagation in Aluminum Alloys," *Fracture*, 1969, Chapman and Hall, London, 1969, p. 754.

15 El-Soudani, S. M., and Pelloux, R. M., "Influence of Inclusion Content on Fatigue Crack Propagation in Aluminum Alloys," *Metallurgical Transactions*, Vol. 4, Feb. 1973, p. 519.

16 Shih, T., and Araki, T., "The Effects of Non-Metallic Inclusions and Microstructures on the Fatigue Crack Initiation and Propagation in High Strength Carbon Steels," *Transactions*

*of the Iron and Steel Institute of Japan*, Vol. 13, 1973, p. 11.

17 Wessel, E. T., Clark, W. G., Jr., Pryle, W. H., "Fracture Mechanics Technology Applied to Heavy Section Steel Structures," *Fracture*, 1969, Chapman and Hall, London, 1969, p. 825.

18 Wessel, E. T., and Mager, T. R., "Fracture Mechanics Technology as Applied to Thick-Walled Nuclear Pressure Vessels," *Practical Application of Fracture Mechanics to Pressure Vessel Technology*, The Institution of Mechanical Engineers, London, 1971, p. 17.

19 Rolfe, S. T., and Novak, S. R., "Slow Bend  $K_{Ic}$  Testing of Medium Strength High Toughness Steels," ASTM STP 463, 1970, p. 124.

---